Copper Oxo Active Sites for Methane C-H Activation in Zeolites: Molecular Understanding of Impact of Methane Hydroxylation on UV-Vis Spectra

Olajumoke Adeyiga, Olabisi Suleiman and Samuel O. Odoh*

Department of Chemistry, University of Nevada Reno, 1664 N. Virginia Street, Reno, NV 89557-0216

Email Addresses:

oadeyiga@unr.edu

osuleiman@unr.edu

sodoh@unr.edu

Abstract: Here, we analyze changes in the optical spectra of activated copper-exchanged zeolites during methane activation with Tamm-Dancoff time-dependent density functional theory, TDA-DFT, while using the ωB2PLYP functional. Two active sites, $[Cu_2O]^{2+}$ and $[Cu_3O_3]^{2+}$, were studied. For $[Cu_2O]^{+}$, the 22700 cm^{-1} peak is associated with μ-oxo 2p → Cu 3d/4s charge transfer. Of the $[Cu_2O]^{2+}$ methane C-H activation intermediates that we examined, only [Cu-O(H)(H)-Cu] and [Cu-O(H)(CH_3)-Cu] have spectra that match experimental observations. After methane activation, the μ-oxo 2p orbitals lose two electrons and become hybridized with methanol C 2p orbitals and/or H 1s orbitals. The frontier unoccupied orbitals become more Cu 4s/4p Rydberg-like, reducing overlap with occupied orbitals. These effects cause the disappearance of the 22700 cm^{-1} peak. For $[Cu_3O_3]^{2+}$, the exact structures of the species formed after methane activation are unknown. Thus, we considered 8 possible structures. Several of these provide significant decrease in intensity near 23000-38000 cm^{-1}, as seen experimentally. Notably, these species involve either rebound of the separated methyl to a μ-oxo atom or its remote stabilization at a Brønsted acid site in exchange for the acidic proton. These spectral changes are caused by the same mechanism seen in $[Cu_2O]^{2+}$ and are likely responsible for the observed reduced intensities near 23000-38000 cm^{-1}. Thus, TDA-DFT calculations with ωB2PLYP provide molecular-level understanding of the evolution of copper-oxo active sites during methane-to-methanol conversion.

Keywords: Copper-exchanged zeolites, UV-vis absorption spectra, $[Cu_2O]^{2+}$, time-dependent density functional theory, mordenite.

1. INTRODUCTION

Methane in natural gas is a source of energy and a starting point for making various chemical intermediates.[1,2] However, due to the expensive nature of storing and transporting natural gas, there is great interest in the development of cheap and environmentally friendly approaches to convert methane to methanol.[3] This conversion of methane to a liquid derivative is one of the holy grails of hydrocarbon chemistry and chemical catalysis. A critical challenge is balancing the requirement of high temperatures or highly reactive substrates to activate the stable methane C-H bond while preventing over-oxidation to species like CO_2 or CO. Interestingly, copper-exchanged zeolites are one of the most exciting species for achieving this conversion at moderate temperatures, albeit in a stoichiometric, rather than catalytic fashion.[4-7] Thus, there has been great interest in understanding the properties of these zeolites. Specifically, there is interest in understanding the nature of the copper-oxo active sites as well as the impact of the zeolite framework's second coordination sphere on methane-to-methanol conversion.[8,9] This has led to many detailed experimental characterizations of the copper-exchanged zeolites, with great interest in the evolution of their properties during the step-wise conversion of methane to methanol. Spectroscopic techniques like X-ray diffraction, NMR, EPR, IR and resonant Raman have been extensively used to study copper-exchanged zeolites. Additionally, UV-Vis/NIR spectroscopy has been used to study the evolution of the copper-oxo active sites during their activation and reaction with methane.[10-26] By activation, we mean high-temperature processes for forming the copper-oxo active sites from Cu^{2+} ions that are typically introduced into the zeolite by ion-exchange methods. In many areas of advanced chemistry, it is common to use quantum-mechanical computational analysis to provide insights and support for experimental spectroscopic data.[27] However, interpretation of the UV-Vis/NIR spectra of copper-exchanged zeolites has not been widespread. This is partly because of the size of the zeolitic systems, necessitating the use of periodic boundary conditions or large cluster models. This limits one's ability to use the highest quality computational methods to study these systems. For this reason, most studies on the optical spectra of copper-exchanged zeolites have used time-dependent linear-response density functional theory (TD-DFT) [28] or Hartree-Fock theory (TD-HF).[29] As examples, Woertink et al. showed that the observed peak at 22700 cm^{-1} in the optical spectrum of the mono-(μ-oxo) dicopper $[Cu_2O]^{2+}$ active site within zeolite ZSM-5 can be reproduced well with TD-DFT calculations while using the B3LYP functional.[30] Li et al. used a combination of ab initio molecular dynamics and TD-DFT to

show the importance of exchange-site heterogeneity and dynamics on the UV-Vis spectrum of copper-oxo dimers and polynuclear species in the SSZ-13 zeolite.[31] Göltl et al. used a novel, parameterized TD-HF-type approach to compute the absorption and photoluminescence spectra of Cu(I) sites in the SSZ-13 zeolite.[32] Also recently, Ipek et al. used Green functions-based methods as well as the Bethe-Salpeter equation[33,34] to compute the optical spectra of the μ-(η^2:η^2) bent-peroxo dicopper $[Cu_2O_2]^{2+}$ in the SSZ zeolite.[35] Interestingly, TD-DFT is far cheaper than the approaches used by Ipek et al. However, TD-DFT calculations on transition metal species are often problematic due to static correlation effects as well as other deficiencies in approximate Kohn-Sham density functionals.[36-38] Some other deficiencies include the presence of ghost excitations, incorrect treatment of charge-transfer effects as well as difficulties associated with handling systems with broken-symmetry open-shell singlet wavefunctions.[28,39,40] Fortunately, there have been significant advances in practical TD-DFT over the last few decades. As such, some of these problems already have some practical solutions.[41] Towards this end, some of us recently reported that a fairly new density functional, ωB2PLYP,[42-44] can provide excellent accuracies for predicting the spectra of several copper-oxo active site motifs implicated in methane-to-methanol conversion, MMC.[45] This functional is a long-range corrected double-hybrid functional. It uses a previously-described configuration-interaction singles and double, CIS(D)-style[42,46,47] scheme to predict electronic transitions, when used for computing absorption spectra.[42-44] The long-range correction allows for good treatment of charge-transfer problems while the corrections for CIS(D)-style scheme might be useful for multi-electron processes. Interestingly, despite the various advances within TD-DFT, there has been no detailed quantum-mechanical description of the changes in the UV-Vis spectra of copper-exchanged zeolites during methane activation.

Here, we use TD-DFT calculations with ωB2PLYP to probe UV-Vis spectra of the mono-(μ-oxo) dicopper $[Cu_2O]^{2+}$ and tris-(μ-oxo) tricopper $[Cu_3O_3]^{2+}$ active sites. Specifically, we report the calculated spectra for these species, before and after reaction with methane. We provide quantum-mechanical insights into how methane activation causes the disappearance of some signature peaks: 22700 cm^{-1} for $[Cu_2O]^{2+}$ and 30000-38000 cm^{-1} for $[Cu_3O_3]^{2+}$.[9,48] This is important for identifying intermediate species involved during stepwise stoichiometric methane activation. Electronic structure understanding of the spectral changes provides a formal description of the evolution of the copper-oxo active sites. Additionally, it is important to ascertain the utility of

ωB2PLYP during methane activation as well as during active site formation and regeneration. This is likely to be very useful in future spectroscopic characterizations of novel active site motifs.

2 METHODOLOGY

2.1. Geometry Optimizations: All cluster models in this work were optimized with the B3LYP[49-51] functional while accounting for dispersion effects with the D3BJ scheme.[52-55] Due to the large number and sizes of the complexes, Figures 1 and 2, we used the def2-SVP basis sets[56] for all atoms. For $[Cu_2O]^{2+}$ and $[Cu_3O_3]^{2+}$ as well as their intra-zeolite methoxy intermediates, we separately optimized the high- and low-spin states. Energies were considered to be converged after reaching 1×10^{-8} a.u. thresholds. These geometry optimizations were performed with the ORCA v4.2.1 software code.[57] Vibrational frequency analyses were carried out analytically to ensure that the optimized structures corresponded to local minima. Most of our optimized structures had only positive vibrational frequencies. In a few cases with imaginary frequencies (less than 200 cm^{-1}), we ascertained that these motions were centered on the terminating protons of the cluster models.

2.2. Electronic Structure Analysis: To analyze the characteristics of the molecular orbitals of the $[Cu_2O]^{2+}$ and $[Cu_3O_3]^{2+}$ cluster models, we considered the Löwdin orbital populations. This maintains the features of Mulliken analysis, without the heavy basis set dependence.

2.3. TD-DFT Calculations: Using the ORCA v4.2.1[57] software code and the Tamm-Dancoff approximation,[58] TDA-DFT, we computed the UV-Vis spectra of all species in Figures 1 and 2 with the ωB2PLYP functional.[42] These calculations were performed with the cc-pVDZ[59-61] basis set. We have shown that TDA-DFT spectra of copper oxo species are largely independent of basis set size.[45] We used the resolution of identity and chain-of-spheres approximation, RIJCOSX,[62] with def2-TZVP[63] auxiliary correlation basis sets. We requested 100-200 states during all TDA-DFT calculations. TDA-DFT spectra for the $[Cu_2O]^{2+}$ and $[Cu_3O_3]^{2+}$ species were fitted with a Lorentzian functions[64] with full widths at half maxima of 1200 and 3500 cm^{-1}, respectively.

3 RESULTS AND DISCUSSIONS

3.1. Dicopper Mono-Oxo $[Cu_2O]^{2+}$ System:

3.1.1. Cluster models: To create a cluster model for $[Cu_2O]^{2+}$, we took this active site and achieved charge neutrality by adding two aluminate tetrahedra to the metal centers. We then added silicate tetrahedra, ensuring a good description of the second-coordination spheres around the metals,

Figure 1. We constructed this model from an optimized unit cell of ZSM-5.[7,12,65,66] The model was extracted from an optimized unit cell with Al atoms placed at the crossing of the straight and sinusoidal pores. There are two T-sites between the Al atoms. Cu centers were arranged near the aluminate tetrahedra in accordance with the descriptions of Tsai et al.[67] and Arvidsson et al.[66] Cu-ZSM-5 has been demonstrated for stepwise and continuous catalytic MMC. The spectroscopic properties of the $[Cu_2O]^{2+}$ active site in this zeolite have also been investigated.

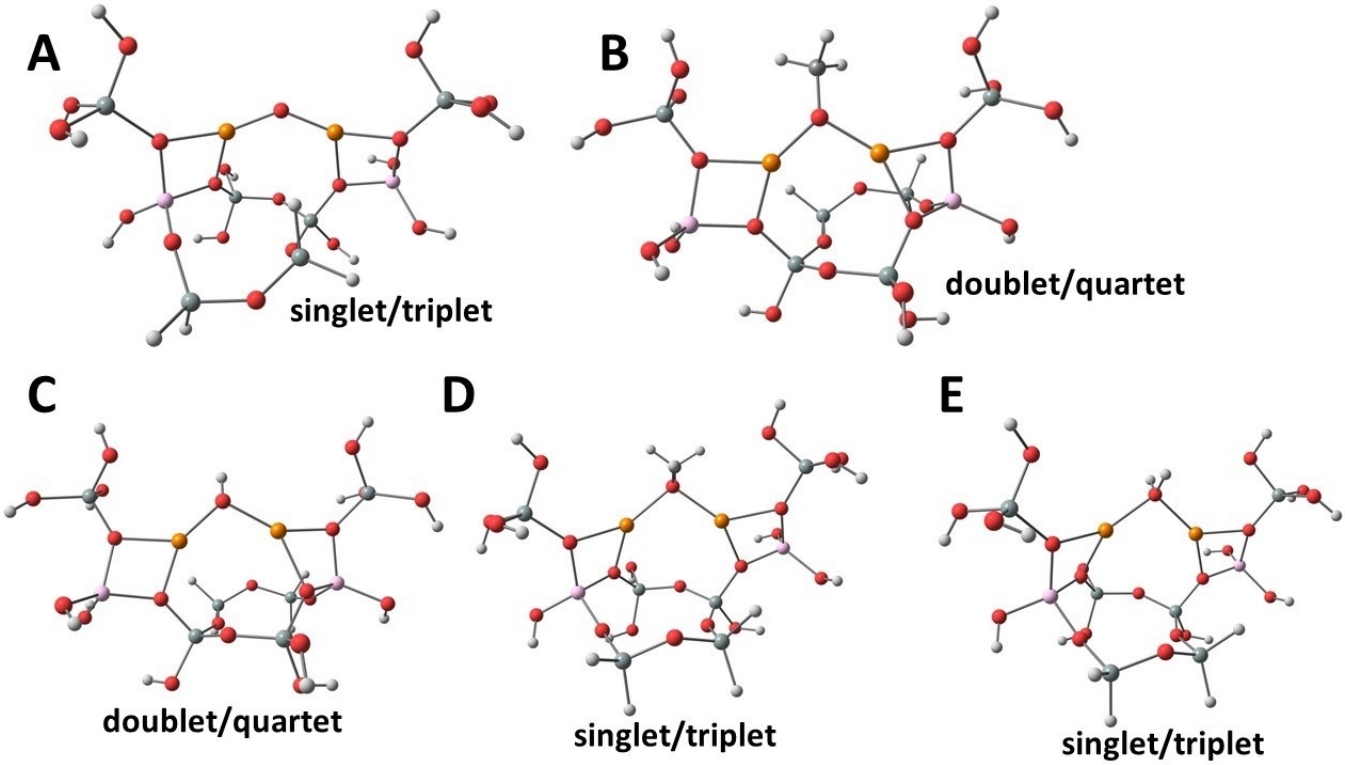

Figure 1: Optimized structures of the cluster models of $[Cu_2O]^{2+}$. **A** is the cluster model for the active site. **B**-**E** are possible intermediates formed after methane C-H activation. The considered spin states are provided.

To examine the impact of methane activation on the spectra of $[Cu_2O]^{2+}$, we considered strongly-bound methanol at the active site. This makes sense as Oord et al.[68] have demonstrated that methane reaction with copper oxo sites is accompanied by detection of vibrational overtones due to $Cu(CH_3)(H_2O)$ or $Cu(CH_3)(OH)$ species.[69] For $[Cu_2O]^{2+}$, the methyl group and proton from methane are bound to the μ-oxo atom, Figure 1. This concurs with the mechanism described by several workers.[66,69-73] Alayon et al. have also proposed the formation of $[Cu\text{-}O(CH_3)\text{-}Cu]^{2+}$ and $[Cu\text{-}O(H)\text{-}Cu]^{2+}$ species with the separated methyl group migrating to another active site, Figure 1b and 1c, respectively. $[Cu\text{-}O(H)\text{-}Cu]^{2+}$ is also relevant if the separated methyl group becomes

stabilized at a Brønsted acid site, BAS. Stabilization of the methyl group could also occur with exchange with an acidic proton. This leads to $[Cu\text{-}O(H_2)\text{-}Cu]^{2+}$ as shown in Figure 1e.

3.1.2. Spin state of $[Cu_2O]^{2+}$ active site: Single point calculations on the optimized structures of the singlet and triplet states of the $[Cu_2O]^{2+}$ cluster model, Figure 1a, reveals that the singlet state is more stable. Indeed with B3LYP, CAM-B3LYP[74] and ωB2LYP, we found that the singlet state is favored over the triplet state by 2.8, 3.0 and 2.6 kcal/mol, respectively. Based on these relative energies, the triplet state will contribute less than 1.2% of the population for the $[Cu_2O]^{2+}$ active site, assuming a Boltzmann population distribution. This agrees very well with the absence of any EPR signal in experiments on copper-loaded ZSM-5 by Groothaert et al.[13] As such, we shall focus most of our discussions on the singlet state.

3.1.3. Ground state electronic structure: The frontier orbitals of the singlet state of the $[Cu_2O]^{2+}$ cluster model are shown in Figure 2. The highest singly occupied molecular orbitals (HSOMOs) are largely made up of μ-oxo 2p atomic orbitals (AOs), albeit with appreciable contributions from Cu 3d AOs. Specifically, in the α-electron manifold, the HSOMO has 72.2% μ-oxo 2p and 12.4% Cu 3d AO contributions. Similarly, the HSOMO in the β-electron manifold is made of 71.5% AO from the μ-oxo 2p and 12.5% from the Cu 3d. We see the same behavior in the next highest SOMOs, HSOMO-1s. In the α-electron manifold, the HSOMO-1 is made up of 38.6% from the μ-oxo 2p, 30.3% from the μ-oxo 2p and 13.8% from the Cu 3d AOs. And in the β-electron manifold, there is 55.6% from the μ-oxo 2p, 11.1% from the μ-oxo 2p and 14.5% from the Cu 3d AOs, Figure 2. On the other hand, the lowest unoccupied molecular orbitals (LUMO) of the $[Cu_2O]^{2+}$ cluster model are largely localized on the Cu centers. In the α-electron manifold, the LUMO contains 33.5% Cu 4s and 38.5% Cu 3d AO contributions. In the β-electron manifold, the LUMO contains 29.4% Cu 4s and 45.1% Cu 3d. Based on this analysis of the frontier molecular orbitals (MOs), excitations from the HSOMOs and HSOMO-1s to the LUMOs will mainly be of μ-oxo 2p → Cu 3d/4s charge transfer character.

3.1.4. Methane activation and electronic structure: After activation of the methane C-H bond, one possible intermediate is strongly-bound methanol is shown in Figure 1d. We chose to analyze the electronic structure of this species (**1d**) due to spectroscopic observations of methanol, after contacting methane with activated zeolites. This is even prior to treatment with water. The frontier orbitals for the singlet state this species are shown in Figure 3. For this species, the singlet state is 39.8 kcal/mol more stable than the triplet state. Interestingly, there are no frontier orbitals with

significant μ-oxo 2p AO contributions after methane activation. Indeed between HSOMO and HSOMO-30, a span of about 4.5 eV (36432 cm^{-1}), the highest μ-oxo 2p contributions to any MO

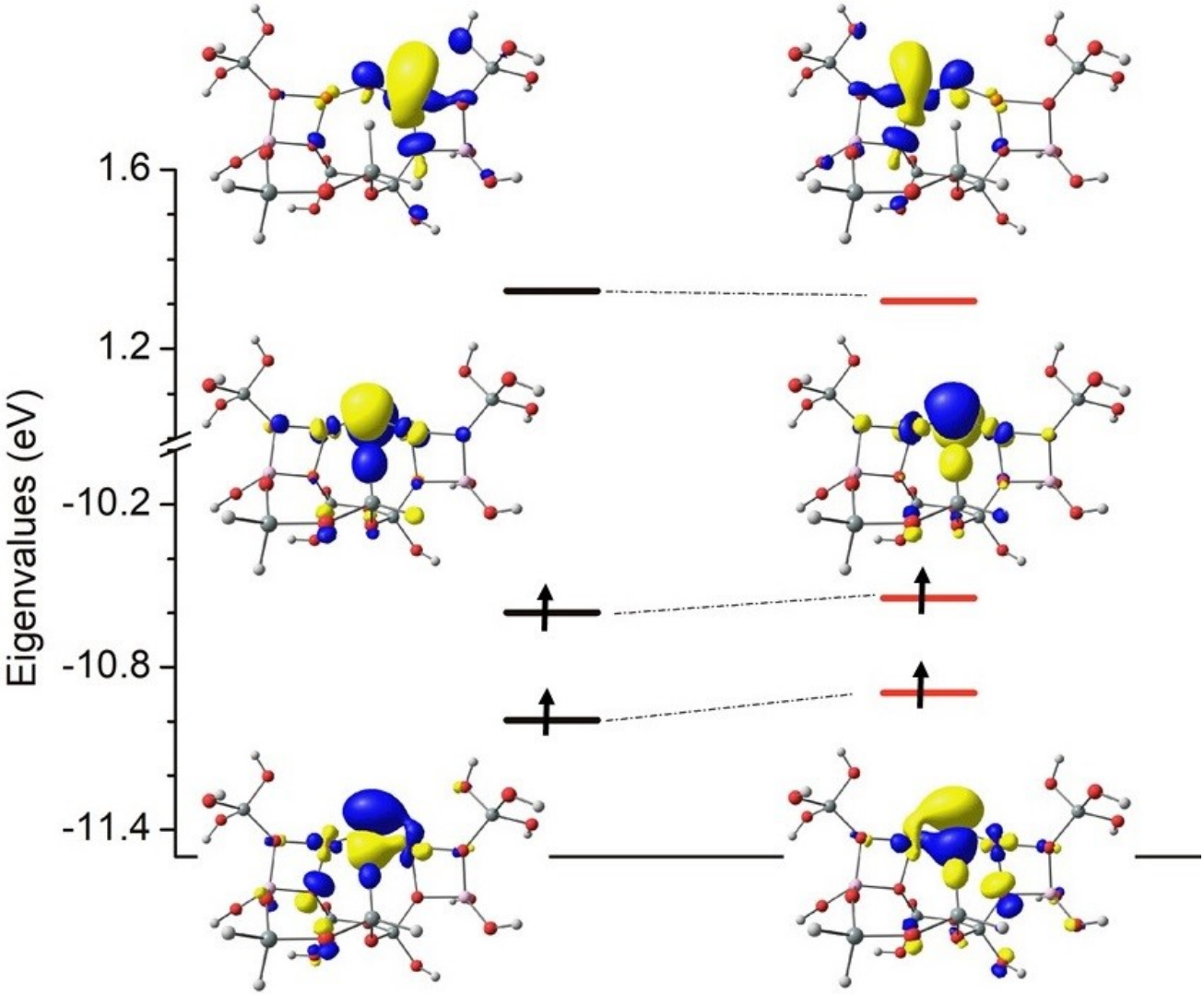

Figure 2: Frontier orbitals of the open-shell singlet ground state of the $[Cu_2O]^{2+}$ cluster model obtained with the ωB2LYP functional and cc-pVDZ basis sets.

are less than 3%. Close examination reveals that the μ-oxo 2p AOs are significantly stabilized due to hybridization with the methyl C 2p AOs. These MOs now have eigenvalues around -16 to -20 eV, Figure 2, in contrast to the situation before methane activation, Figure 2, where they have eigenvalues of around -11 eV. Thus, the nature of the HSOMO and HSOMO-1 have dramatically changed. After methane activation, these are now predominantly Cu based. As example, HSOMO contains 52.2% contribution from Cu 3d AOs. Interestingly, the LUMOs are now predominantly of Cu 4s and 4p character after methane activation. Indeed, there are very little contributions from

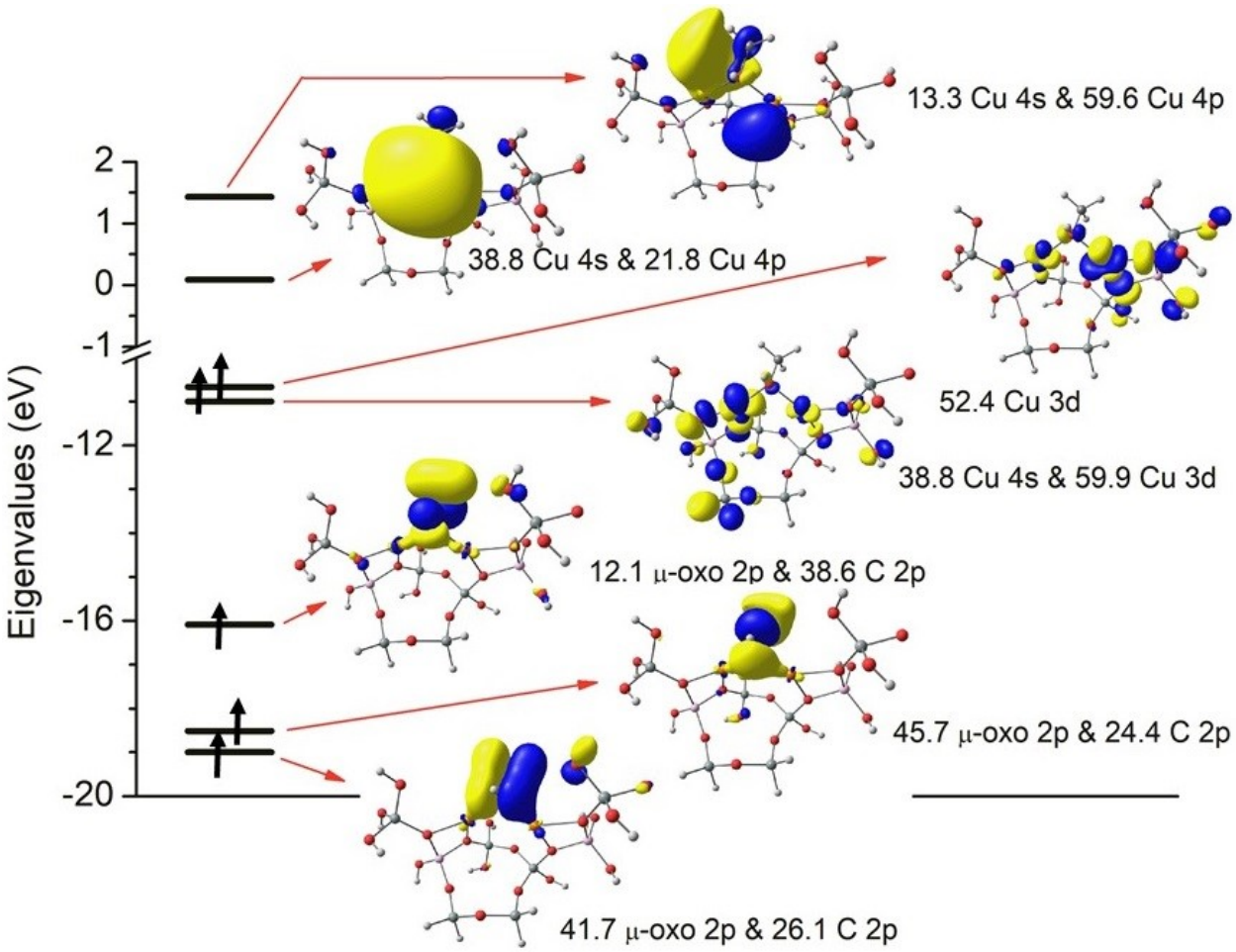

Figure 3: Frontier orbitals of the open-shell singlet ground state of the $[Cu_2O]^{2+}$ active site after methane activation. These were obtained at the ωB2LYP/cc-pVDZ level.

Cu 3d AOs to the LUMOs, a stark contrast to the situation before methane activation.

Based on the stabilization of the C 2p and O 2p hybrid orbitals; the 3d character of HSOMO and HSOMO-1; as well as significant 4p character of the LUMOs, Figure 3, we conclude that methane activation is accompanied by electron transfer from MOs with significant μ-oxo 2p AO character to MOs with significant Cu 3d character. This indicates a 2-electron reduction of both Cu^{2+} centers in $[Cu_2O]^{2+}$ [$2Cu^{2+} \rightarrow 2Cu^{+}$ or $2Cu^{2+} \rightarrow Cu + Cu^{2+}$, depending on the exchange-correlation density functional]. Additionally, the significant contribution of 4p AOs to the LUMOs after methane activation is indicative of a more diffuse and Rydberg-like character, see Figures 2 and 3. This would suggests poor spatial overlap during electronic transitions involving these orbitals. Thus, it is reasonable to expect that methane activation will lead to significant reduction in the oscillator strengths of transitions to the low-lying Cu 4s and 4p LUMOs.

3.1.5. Methane activation and TDA-DFT spectra: The spectra obtained at the ωB2PLYP/cc-pVDZ level for the $[Cu_2O]^{2+}$ cluster model before (Figure 1a) and after methane activation (Figure 1b-d) are shown in in Figure 4. Before methane activation, there is a prominent calculated feature at 22889 cm^{-1}, in great agreement with the experimental band at 22700 cm^{-1}. We and Woertink et al. have previously described this feature as being due to μ-oxo 2p → Cu 3d/4s charge transfer.[30,45] Indeed, it is specifically due to transitions from the μ-oxo 2p HSOMO and HSOMO-1 to the Cu 4s/3d LUMO, Figure 3. The difference density illustrates clearly the charge-transfer nature of this

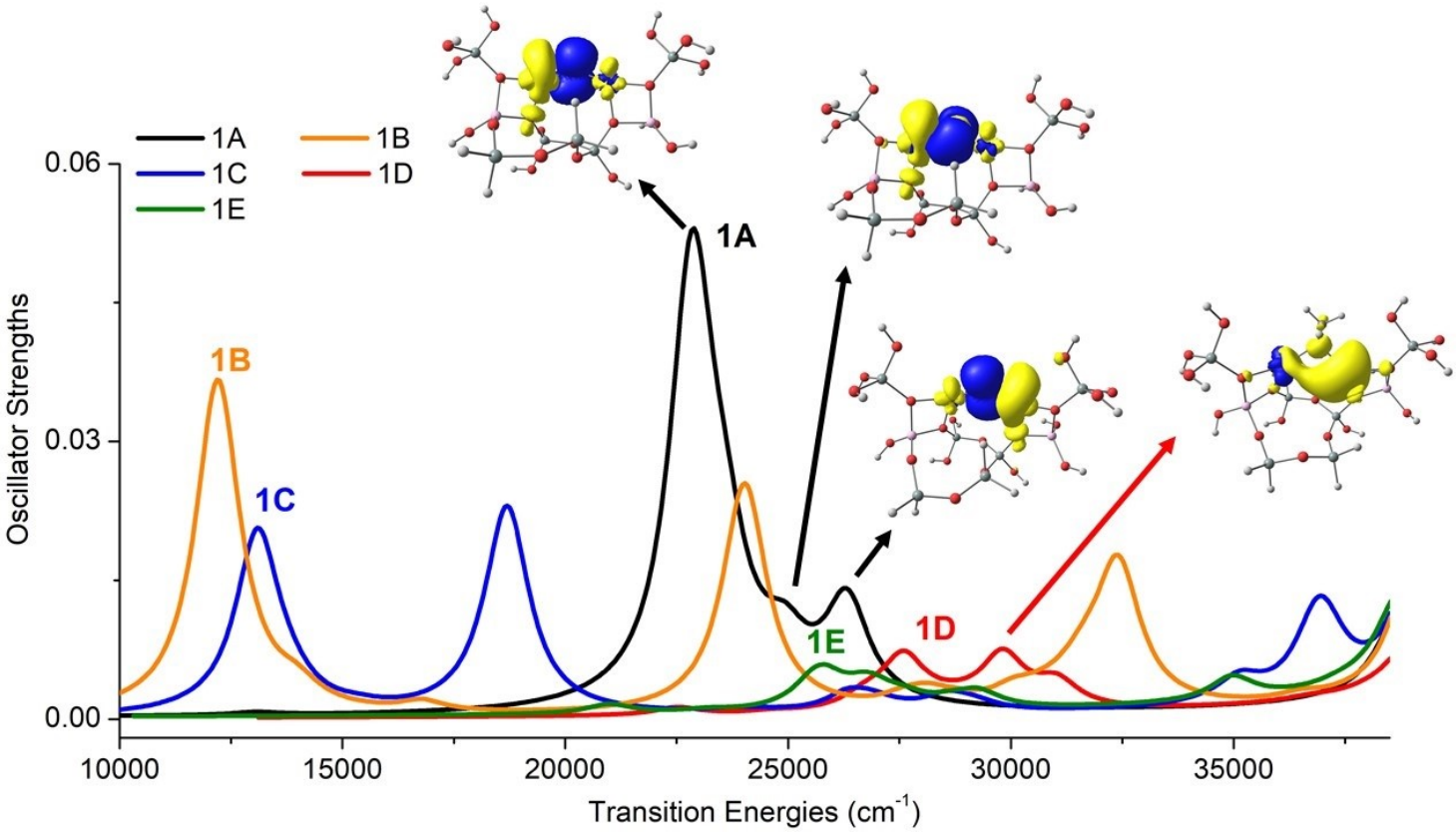

Figure 4: Calculated spectra obtained at the ωB2PLYP/cc-pVDZ level for the $[Cu_2O]^{2+}$ cluster model and possible intermediates after methane activation. The difference densities between the ground and excited states are shown as insets.

transition, see inset of Figure 4. Indeed, the difference density reveals depletion of electron density on the μ-oxo atom (blue color) and aggregation of electron densities in the excited state on the Cu centers (yellow). In addition to the feature at 22889 cm^{-1}, TDA-DFT also yields a significantly less intense charge-transfer peak at 26307 cm^{-1}. Moreover, Groothaert reported a signature 22700 cm^{-1} peak as well as a relatively weaker band near 30000 cm^{-1} in their characterization of O_2-activated Cu-ZSM-5. Thus, our calculations agree quite well with experimental data.

After methane C-H activation, the features at 22889 and 26307 cm^{-1} have disappeared in the intermediate with strongly bound methanol, **1d**. There are now only minor peaks at 27566, 29841 and 31063 cm^{-1}, Figure 4. As noted earlier, these are weaker as they involve transitions to Cu 4s/4p diffuse Rydberg-type orbitals, Figure 3. The energy shift is due to the fact that the nature of the occupied frontier orbitals changed dramatically upon methane activation, Figures 3 and 4. Interestingly, the disappearance of the 22700 cm^{-1} feature from the experimental UV-Vis spectra of O_2-activated Cu-ZSM-5 has been used to monitor the kinetics of methane activation.[30] Therefore, ωB2PLYP can reproduce these experimental observations as well as furnish a molecular-level understanding of the peak's disappearance.

Interestingly, Figure 4 shows that both **1c** also has reduced intensities in the 20000-35000 region. However, it now features lower-energy transitions below 20000 cm^{-1}. This is also the case for **1b**. The new features below 20000 cm^{-1} and in the case of **1b**, around 32300 cm^{-1}, have not been reported experimentally. On the other hand, **1e** features reduced intensities near 20000 cm^{-1} and has no new features, just like **1d**. Examination of the electronic structures of **1e** reveals similar stabilization of the frontier MOs with μ-oxo 2p AOs character as well as presence of significant 4s/4p character of the LUMOs, as was seen for **1d**. Similarity between the spectra of **1d**, and **1e** shows a limitation of UV-Vis spectroscopy; experimental observations could be due to multiple intra-zeolite intermediates.

3.2. Tricopper Trioxo $[Cu_3O_3]^{2+}$ System:

3.2.1. Cluster models: To create a cluster model for $[Cu_3O_3]^{2+}$, we took the metal oxo core and added two aluminate tetrahedra to the first coordination sphere of the metals, Figure 5. This leads to a cluster model of the 8MR of zeolite mordenite (MOR). This model has been previously used to study methane over-oxidation as well as electronic structure and spectroscopic properties of $[Cu_3O_3]^{2+}$. Additionally, many claims of unique preparations of the tricopper site have been for copper-exchanged MOR.

For $[Cu_3O_3]^{2+}$, the exact natures of the intermediates formed after methane activation are unknown. As such, we have considered various arrangements of the methyl and proton around the active site, Figure 5b-i. First, we considered situations where the separated proton and methyl groups are sited at different μ-oxo atoms (**5b**, **5c** and **5d**). The methyl could also rebound to the reactive μ-oxo atom (**5e** and **5f**). Interestingly, recent experimental and theoretical reports have suggested that the methyl group is actually not stabilized at the active site. Several workers have

shown that the methoxy is formed at Brønsted acid sites.[75-77] We have also shown that stabilization of the methyl at the active site is a recipe for over-oxidation.[78,79] Considering these, we optimized the geometries of other possible structures. First, the methyl group could be stabilized away from the active site. This leads to structure **5g** in Figure 5g. Conversely, the methyl could be stabilized on framework aluminates in exchange for a proton. This proton can be located at a new μ-oxo atom (**5h**) or at the reactive μ-oxo atom (**5i**).

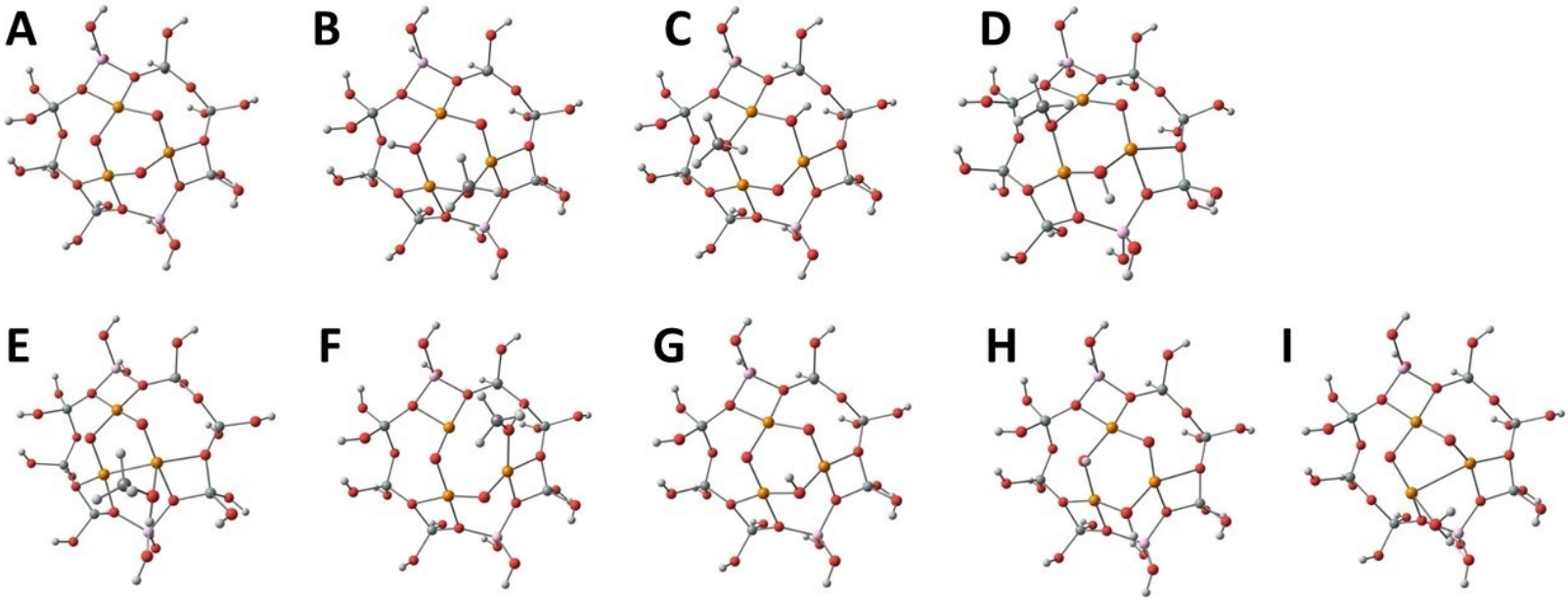

Figure 5: Optimized structures of the cluster models of $[Cu_3O_3]^{2+}$. **A** is the cluster model for the active site. **B**-**I** are possible intermediates formed after methane C-H activation. The ground spin states of these species are provided.

3.2.2. Spin state of $[Cu_3O_3]^{2+}$ active site: We previously discussed that GGA density functionals predict the doublet state of the $[Cu_3O_3]^{2+}$ active site is more stable the high-spin quartet state.[80] Vogiatzis et al. reported that the energy difference between the doublet and quartet states is consistent between GGA functionals and multireference methods.[81] As such, we shall focus our discussions on the doublet state of our cluster model, Figure 5a.

3.2.3. Ground state electronic structure: The frontier orbitals of the singlet state of the $[Cu_3O_3]^{2+}$ cluster model are shown in Figures 6 and 7. In the α-spin manifold, the HSOMO consists largely of 2p AOs from two μ-oxo atoms of the $[Cu_3O_3]$ core; 79.4% 2p AOs from both. It also contains 6.4% from Cu 3*d* AOs, Figure 7. A similar situation is seen for HSOMO-1; 71.8% μ-oxo and 7.8 % 3d. HSOMO-2 has significant 2p contributions from an aluminate oxo group, Figure 6. However, the second largest contribution to this orbital is from μ-oxo 2p AOs. The dominance

of the μ-oxo 2p AOs in the frontier α-spin orbitals extends to HSOMO-3 and HSOMO-4. HSOMO-4 has 36% contribution from μ-oxo 2p AOs as well as 8.9% from Cu 3d AOs from Cu. It also has about 33.6% contribution from an aluminate oxo group. The LUMO has some antibonding character containing also 74.9% 2p AO contributions from two μ-oxo atoms. It also contains a minor contribution of 4.0% from Cu 4p orbitals. The LUMO+1 orbital is however dominated by Cu 4s and 4p AOs; 46.2 and 5.6% respectively.

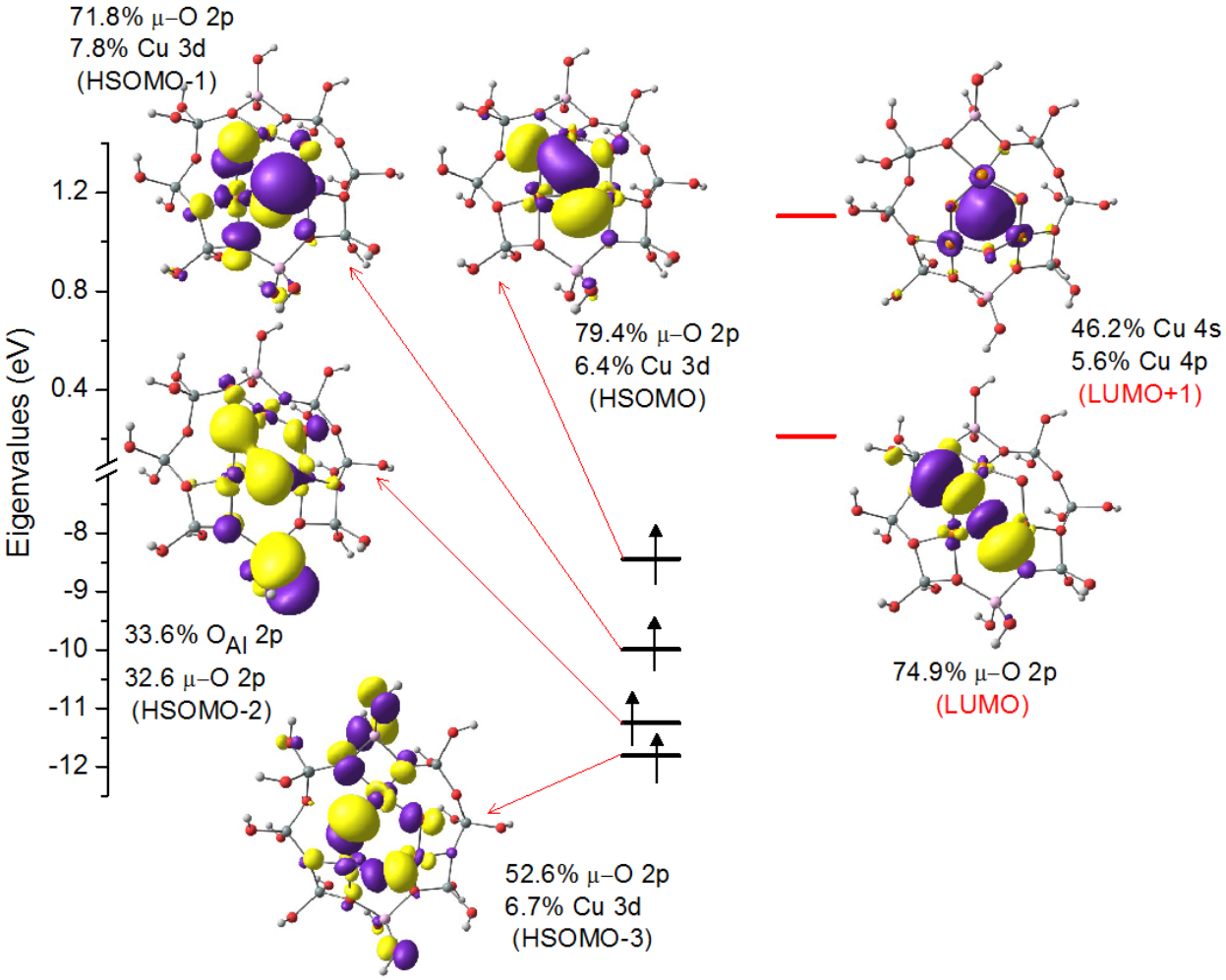

Figure 6: Frontier α-orbitals of the $[Cu_3O_3]^{2+}$ cluster model at ωB2LYP/cc-pVDZ level.

Examination of the β-spin orbitals shows that the LUMO+1 is also largely centered on the Cu centers, with 45.7% Cu 4s and 4.2% Cu 3d. The LUMO, HSOMO and HSOMO-1 are however dominated by μ-oxo 2p AOs, just like for the α-spin orbitals. Based on Figures 6 and 7, we can conclude that excitations into the LUMOs will be of μ-oxo 2p → 2p character. Excitations into LUMO+1 will have significant ligand-to-metal charge transfer character (μ-oxo 2p → Cu 4s).

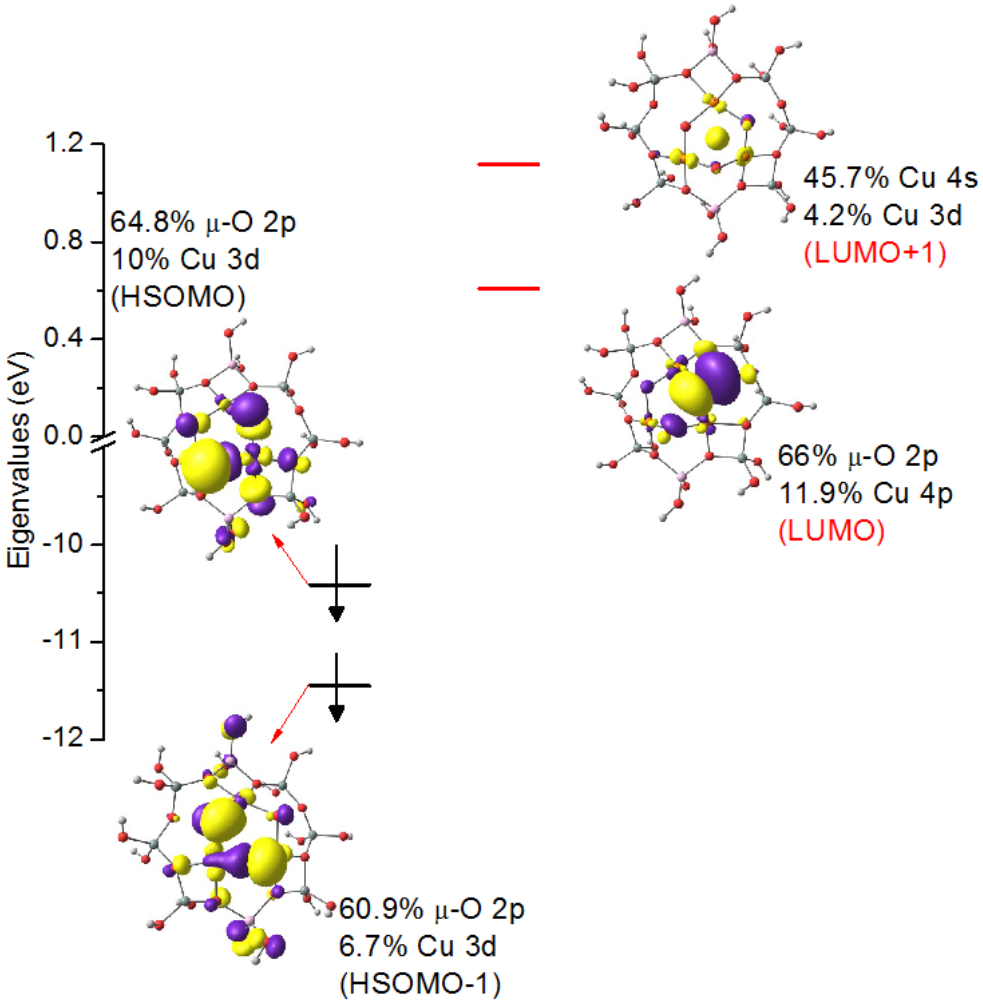

Figure 7: Frontier β-orbitals of the $[Cu_3O_3]^{2+}$ cluster model at ωB2LYP/cc-pVDZ level.

3.2.3. Methane activation and TDA-DFT spectra: Several workers have examined methane activation by the $[Cu_3O_3]^{2+}$ active site in the 8MR of MOR. It was reported that the reflectance of the band near 31000 cm^{-1} decreases after contact with methane.[9,48,82] Indeed, a difference spectrum reported by Ikuno et al. showed reduction for features between 23000 and 38000 cm^{-1}.[82] As stated earlier, the exact natures of the intermediate species formed after methane activation by $[Cu_3O_3]^{2+}$ are somewhat unknown. For this reason, the TDA-DFT spectrum of **5a** is compared to spectra for **5b-5i** in Figures 8 and 9. Assignment of the spectral features of the $[Cu_3O_3]^{2+}$ active site, **5a**, is presented in Table 1. We highlight that unlike the features at 14530, 25383 and 30110 cm^{-1}, the peaks at 34139 and 36563 cm^{-1} have significant contributions from Cu-centered 4s, 4p and 3d AOs in the relevant virtual orbitals.

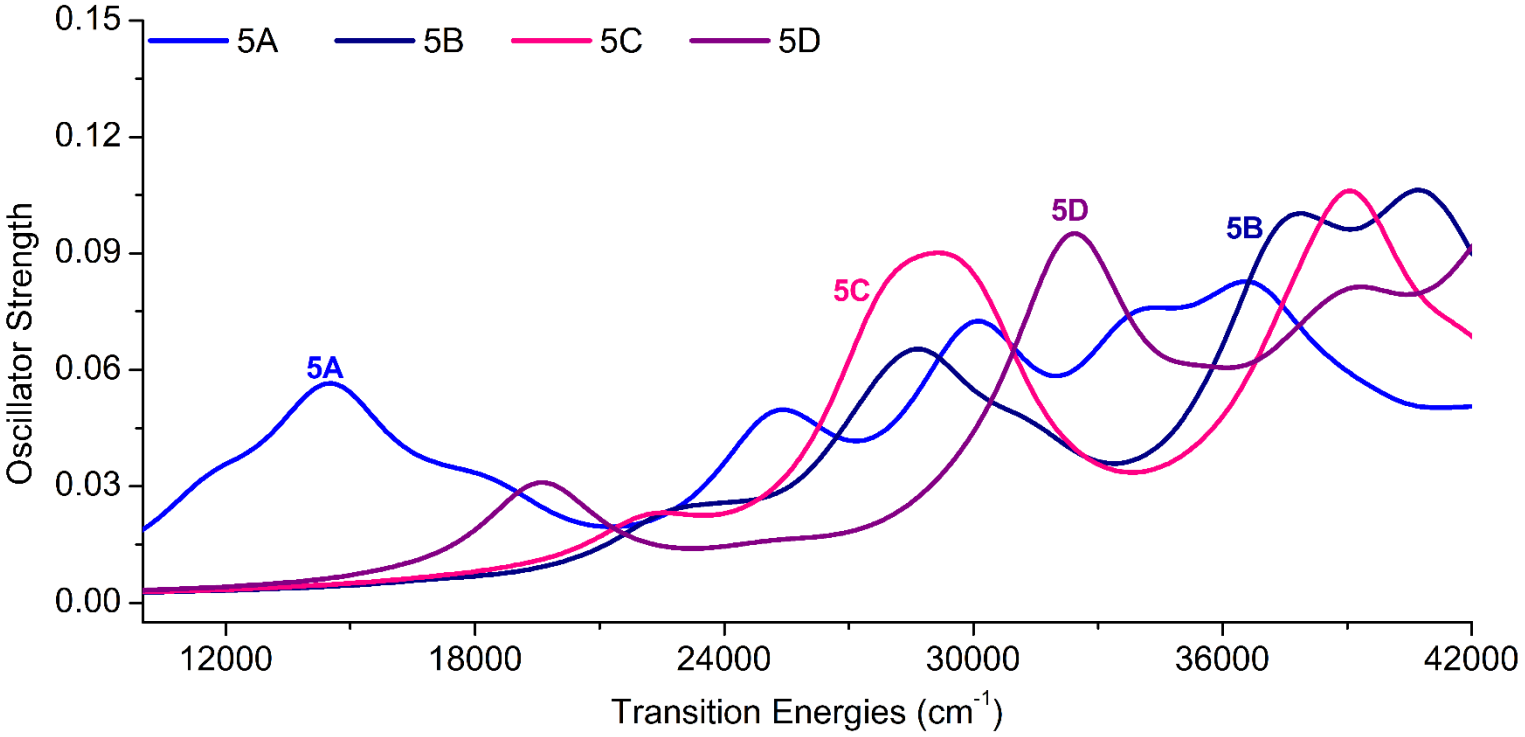

Figure 8: Comparison of calculated spectra of $[Cu_3O_3]^{2+}$ to several possible intermediates for methane activation, **5b-5d**.

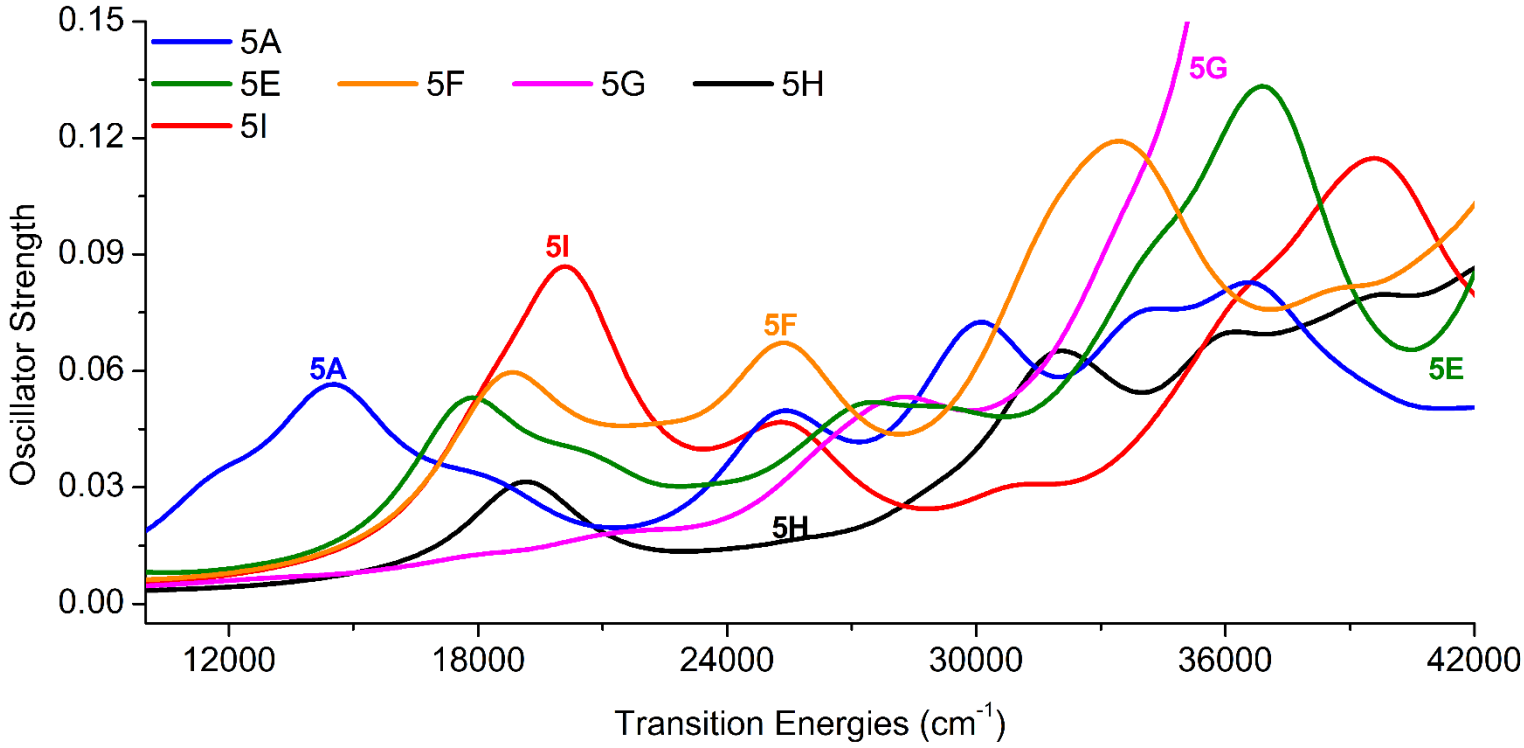

Figure 9: Comparison of calculated spectra of $[Cu_3O_3]^{2+}$ to several possible intermediates for methane activation, **5e-5i**.

Table 1: Characters of the dominant excitations, in cm^{-1}, in the TDA-DFT spectrum of $[Cu_3O_3]^{2+}$.

Calculated		Experiment	Largest contributions	Character
Major Peak	Constituents			
14530		10000-2000	α-HSOMO → LUMO	μ-oxo 2p → μ-oxo 2p
25383		~ 24000	α-HSOMO-2 → LUMO	framework → active-site CT
30110		~ 31000	α-HSOMO-4 → LUMO	framework → active-site CT
34139		~ 34000	β-HSOMO → LUMO and α-HSOMO → LUMO+1	μ-oxo 2p → μ-oxo 2p and μ-oxo 2p → Cu 4s
36563	36448	~ 38500	β-HSOMO → LUMO+1	μ-oxo 2p → Cu 4s/3d
	37002		β-HSOMO-1 → LUMO	μ-oxo 2p → μ-oxo 2p and Cu 4p

There are a couple of important things to note regarding the spectra shown in Figures 8 and 9. First, the peak at 14530 cm^{-1} has disappeared in most of the intermediate species. This suggests that the absorbance of the feature near 12000 cm^{-1} should decrease after methane activation. However, the behavior of the feature at 12000 cm^{-1} in the experimental data appears to depend on the set up. Several workers have reported a modest decrease in the reflectance of this region after methane activation.[9,82] Others have reported an increase.[82] All experimental reports are however consistent regarding decrease in the reflectance of the 23000-38000 cm^{-1} region. As such, we shall focus our emphasis on this region.

Second, of the possible intermediates that we considered, only **5b**, **5c**, **5d** and **5h** show lower oscillator strengths in portions of the 23000-38000 cm^{-1} region, Figures 8 and 9. We repeat that in **5b-d**, the methyl rebounds to the active site whereas in **5h**, the separated methyl is exchanged with a Brønsted acid proton, Figure 5. These 2 possibilities have emerged as candidates for the stabilized strongly-bound methoxy.[75,76,78,79,83-85] Examination of the calculated spectra shows that **5b**-**c** predict substantial decrease in the intensities at 23000-25000 cm^{-1} and 30000-36000 cm^{-1}. They however have higher intensities near 29000 cm^{-1}. **5d** has higher intensities than **5a** near 32500 cm^{-1}, Figure 8. **5h** has similar intensities as **5a** near 32000 cm^{-1}, Figure 9. For **5b-d** and **5h**, the intensities are also higher in the regions above 39000 cm^{-1}. Overall, the intensities for **5h** are more consistently lower than for **5a** across the whole 23000-38000 cm^{-1} region.

Other possible intermediates have higher intensities in the 23000-38000 cm^{-1} region. For example, **5e** predict significantly higher intensities near 37000 cm^{-1}. Also **5i** predicts a huge jump in intensity near 20000 cm^{-1}. These do not conform to the experimental findings.[9,48,82]

Based on these considerations, we focus subsequent discussions on **5h**. We again repeat that recent experimental results have shown that the separated methyl group is stabilized at BASs.[75,76,85] Quantum-mechanical computations have shown that exchange of the acidic proton of a BAS with the methyl is indeed energetically feasible.[79] Stabilization of the acidic proton at the active site μ-oxo atom and the methyl at a basic framework aluminate has been shown to be a crucial mechanism for avoiding over-oxidation.[75,78] All of these point towards **5h**.

3.2.4. Impact of structural dynamics: We performed ab initio molecular dynamics (AIMD) simulations on the periodic structure of **5h** at 300 K. After equilibration for 8 ps, we performed 3 simulations of 8 ps length, starting from 3 different structures. From the resulting trajectories, we randomly selected 5 structures of each. These were truncated to the size of the species in Figure 5. Dangling oxygen atoms were capped with protons and positions of the protons were optimized. Full details are provided in the Supporting Information. We then computed the UV-Vis spectra at the ωB2PLYP/cc-pVDZ level. These are compared with spectra for the optimized structure at 0 K in Figure 10 and in the Supporting Information.

Overall, the clusters from AIMD display the same general property as the DFT-optimized structure. They all have lower intensities near the 23000-38000 cm^{-1} region than **5a**. Some of these AIMD clusters also shift the 19000 cm^{-1} feature of **5h** to lower energies; to near 17500 cm^{-1} in the case of **5h-3**, as an example, Figure 10. However, like the DFT-optimized structure,

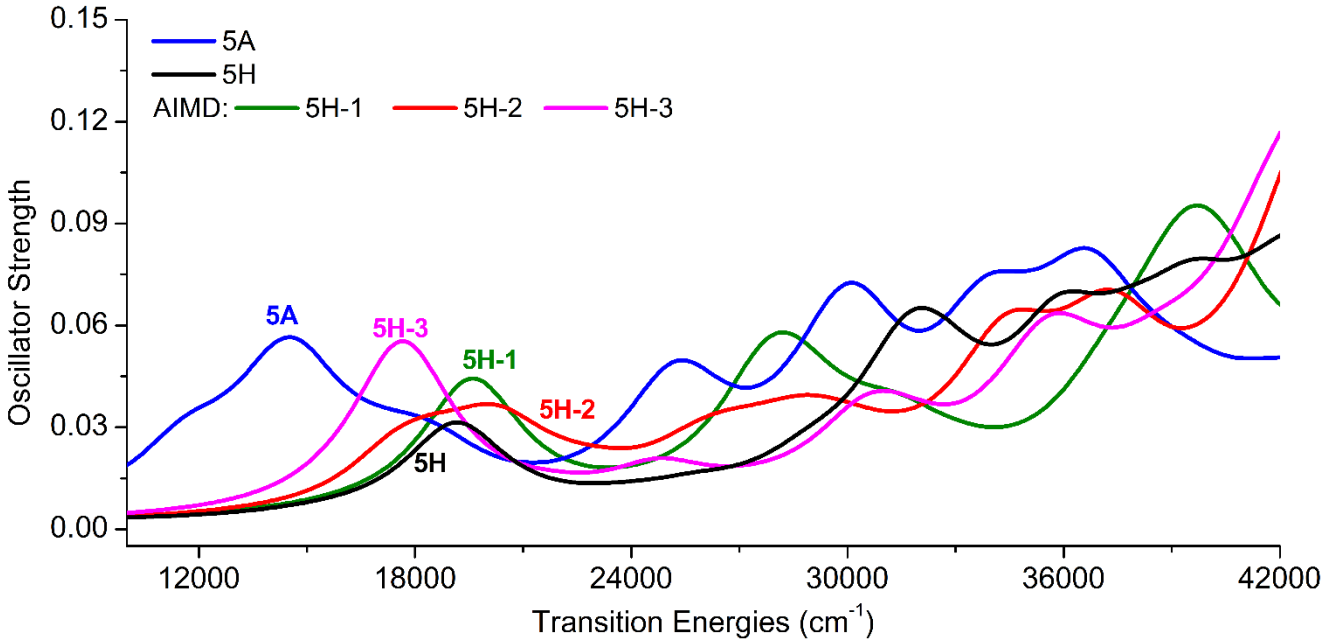

Figure 10: TDA-DFT spectra of cluster models of **5h** obtained from AIMD simulations (1-3) are compared to geometry optimized models for **5a** and **5h**.

all the AIMD species feature higher intensities beyond 38000 cm^{-1} than **5a**.

3.2.5. Methane activation and Electronic Structure: The frontier orbitals of **5h** are presented in Figure 11. Before methane activation, there were 6 μ-oxo 2p-dominated MOs, containing 6 electrons. Two of these had significant σ-type character, with associated unoccupied σ*-type orbitals, Figures 7 and 8. As discussed earlier, transitions between these orbitals are responsible

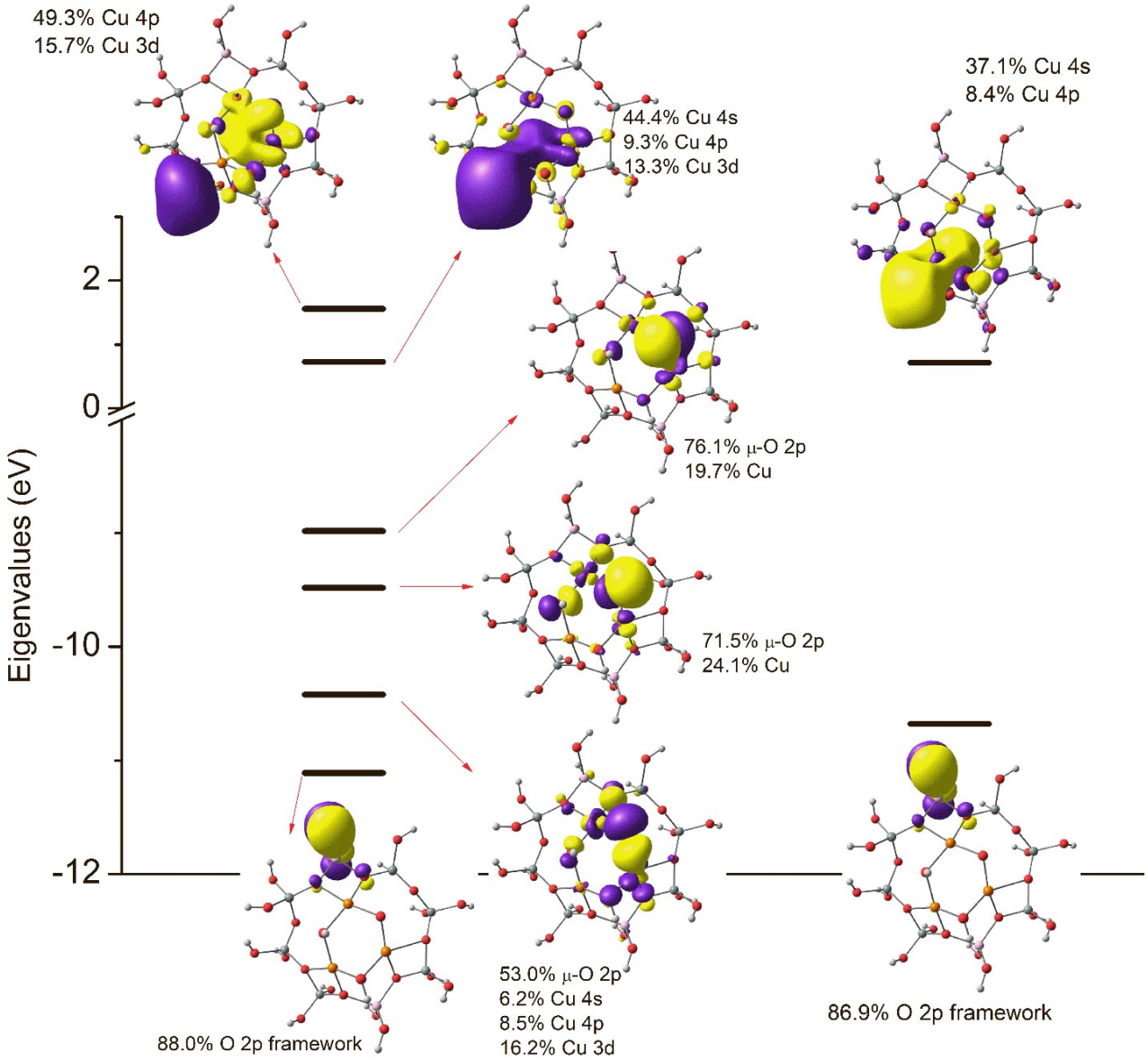

Figure 11: Frontier orbitals of the doublet state of the $[Cu_3O_3]^{2+}$ active site after methane activation to form structure **5h**. These were obtained at the ωB2LYP/cc-pVDZ level.

for the peak at 14530 cm^{-1}. Crucially, after methane activation, some μ-oxo 2p-dominated orbitals still remain in the frontier region, albeit with significantly higher contributions from Cu 3d and Cu 4p orbitals. Specifically, the α-spin HSOMO, HSOMO-1, HSOMO-2 orbitals of **5**h

have 19.7%, 24.1% and 30.9% contributions from Cu AOs, respectively, Figure 11. Indeed, after formation of **5h**, the σ*-type μ-oxo 2p orbitals are no longer in the frontier region. The frontier region is now thoroughly dominated by orbitals with significant Cu character, rather than μ-oxo 2p. In Figure 11, we show that the α-spin LUMO has 67% AOs contribution from Cu while the LUMO+1 has 65%. Similarly, the β-spin LUMO has 66.9% contribution from Cu AOs. We are to compare these with the α-spin and β -spin LUMOs for **5a** which contain 74.9% and 66.0% from **Cu AOs**, respectively. Close examination of Figures 6, 7 and 11 also indicate that the frontier virtual orbitals of **5h** are more unstable (more positive eigenvalues) than those of **5a**. Also, the frontier occupied orbitals of **5h** are more stable (more negative eigenvalues) than those of **5a**. These findings are quite similar to those of the $[Cu_2O]^{2+}$ system, see Sections 3.1.4 and 3.1.5. The significant contribution of Cu AOs to the LUMOs after methane activation (indicative of a more diffuse and Rydberg-like character) and stabilization of frontier μ-oxo 2p occupied orbitals suggests poor spatial overlap during transitions between these orbitals. Thus, methane activation leads to significant reduction in the oscillator strengths of transitions to the low-lying Cu-based LUMOs. We also expect a shift to higher transition energies.

Table 2 shows the assignment of the calculated spectral features of **5h**. A peak at 19128 cm^{-1} contains excitations from the μ-oxo 2p occupied orbitals α-HSOMO-1 to HSOMO, LUMO and LUMO+1. These final orbitals have significant contributions from Cu AOs. Thus, compared to **5a**, this peak is shifted to higher energies and is less intense. The same phenomenon plays out across the 23000-38000 cm^{-1} region. The intensities for **5h** are thus lower than that of **5a** across this region. Interestingly, beyond 38000 cm^{-1} the intensities of **5h** are larger than for **5a**, Figure 9. For **5a**, the computed peak at 36563 cm^{-1} underestimates the experimental feature near 38500-41000 cm^{-1}. Thus, one would expect that based on Figure 11, the absorption intensities of the intra-zeolite intermediates would exceed that of $[Cu_3O_3]^{2+}$ beyond the 38500-41000 cm^{-1} region.

Table 2: Characters of the dominant excitations, in cm^{-1}, in the TDA-DFT spectrum of **5h**.

Calculated	Largest contributions	Character
19128	α-HSOMO-1 → HSOMO, LUMO & LUMO+1	μ-oxo 2p → μ-oxo 2p; Cu 4s, 4p 3d
32090	β-HSOMO-2 → HOMO	framework → active-site CT
36238	α-HSOMO-2 → HOMO	μ-oxo 2p → μ-oxo 2p
39521	α-HSOMO-3 → HOMO and β-HSOMO-3 → HOMO	framework → μ-oxo 2p

CONCLUSIONS

The UV-Vis spectra of copper-oxo active sites within copper-exchanged zeolites are analyzed with cluster-model Tamm-Dancoff time-dependent DFT (TDA-DFT) calculations. These systems are of interest due to their ability to activate the methane C-H bond, selectively converting it to methanol. Specifically, TDA-DFT calculations with ωB2PLYP were used to probe evolution of electronic structure properties and optical spectra of the $[Cu_2O]^{2+}$ and $[Cu_3O_3]^{2+}$ active sites during methane activation. We provide molecular-level understanding of changes in the UV-Vis spectra of copper-exchanged zeolites after contact with methane.

It is established that prior to methane activation, ωB2PLYP provides great agreement with the experimental optical spectra of $[Cu_2O]^{2+}$ and $[Cu_3O_3]^{2+}$. Particularly for $[Cu_3O_3]^{2+}$, it provides bands at 14530, 25383, 30110, 34139 and 36563 cm^{-1}, in agreement with experimental features near 12000, ~24000, 31000, 34000 and 38500-40000 cm^{-1}. The signature peak observed for $[Cu_2O]^{2+}$ at 22700 cm^{-1} is predicted to be at 22889 cm^{-1} with ωB2PLYP. The less intense feature near 30000 cm^{-1} in the experimental data is also captured with ωB2PLYP.

After methane activation by $[Cu_2O]^{2+}$, the calculated optical of [Cu-O(H)(H)-Cu] and [Cu-O(H)(CH_3)-Cu] clearly show a disappearance of 22889 cm^{-1} feature. By contrast, the spectra for [Cu-O(H)-Cu] and [Cu-O(CH_3)-Cu] either do not lead to sufficient reduction of the 22889 cm^{-1} feature or also provide extraneous new features in the 10000-20000 cm^{-1} region. These new features are in great disaccordance with previously reported experimental data. In [Cu-O(H)(H)-Cu] and [Cu-O(H)(CH_3)-Cu], electrons in the μ-oxo 2p-dominated orbitals of $[Cu_2O]^{2+}$ become stabilized and hybridized with C 2p and/or H 1s orbitals from the separated methyl and proton of methane. Electronic structure analysis show a clear transfer of 2 electrons to the copper centers. This dramatically changes the nature of the low-lying unoccupied orbitals. Specifically the μ-oxo 2p contributions to low-lying unoccupied orbitals are removed. Additionally, contributions from Cu 4s and 4p atomic orbitals to these orbitals become dramatically higher. The virtual orbitals thus acquire a more diffuse Rydberg-like character, leading to decreased spatial and/or energy overlaps with the occupied valence orbitals. These effects shift the energies and leads to a dramatic decrease in the oscillator strengths of the 22889 cm^{-1} feature. This concurs with the disappearance of the 22700 cm^{-1} band after methane activation, as seen in our TDA-DFT spectra and previous experimental data.

For the more complicated $[Cu_3O_3]^{2+}$ system, previous reports stated that methane activation is associated with a decrease in intensity in the 23000-38000 cm^{-1} region. However, the exact structure of the intermediate species formed after methane activation by $[Cu_3O_3]^{2+}$ is unknown. Using a set of 8 possible structures, we found that several structures exhibited reduced oscillator strengths in parts of the 23000-38000 cm^{-1} region. Interestingly, these species correspond to rebound of the methyl group to an active site μ-oxo atom or remotely in exchange for a Brønsted acid proton. Recent experimental and theoretical studies have described how stabilization of the methyl at Brønsted acid sites is crucial for preventing over-oxidation. Our TDA-DFT results are thus another evidence supporting such assertions. To understand the lower intensities in the 23000-38000 cm^{-1} region, we discovered that a similar phenomenon as seen in $[Cu_2O]^{2+}$ results in shifting the spectra to higher energies and lower intensities (predominance of Cu atomic orbital contributions in the low-lying virtual orbitals as well as stabilization of the frontier occupied orbitals due to hybridization with H 1s orbitals).

Thus, we conclude that ωB2PLYP is useful for studying the UV-Vis spectra of copper-oxo active site species implicated in methane-to-methanol conversion. It is capable of describing the evolution of these species during the conversion process. Using this approach, we gain a molecular-level understanding into the properties of copper-oxo species implicated in methane-to-methanol conversion.

ASSOCIATED CONTENT

Supporting Information.

The Supporting Information is available free of charge at https://

Optimized geometries of all systems considered in this work (PDF).

AUTHOR INFORMATION

Corresponding Authors

*S.O.O.: E-mail: sodoh@unr.edu

ACKNOWLEDGMENT

This material is based upon work supported by the National Science Foundation under Grant No. 1800387.

REFERENCES

(1) Dunn, S. Hydrogen futures: toward a sustainable energy system, *Int. J. Hydrogen Energ,* **2002**, *27*, 235.

(2) Muradov, N. Z.; Veziroglu, T. N. From hydrocarbon to hydrogen-carbon to hydrogen economy, *Int. J. Hydrogen Energ,* **2005**, *30*, 225.

(3) Lunsford, J. H. Catalytic conversion of methane to more useful chemicals and fuels: a challenge for the 21st century, *Catal. Today* **2000**, *63*, 165.

(4) Narsimhan, K.; Iyoki, K.; Dinh, K.; Román-Leshkov, Y. Catalytic Oxidation of Methane into Methanol over Copper-Exchanged Zeolites with Oxygen at Low Temperature, *ACS Cent. Sci.* **2016**, *2*, 424.

(5) Alayon, E. M.; Nachtegaal, M.; Ranocchiari, M.; van Bokhoven, J. A. Catalytic conversion of methane to methanol over Cu-mordenite, *Chem. Commun.* **2012**, *48*, 404.

(6) Alayon, E. M. C.; Nachtegaal, M.; Ranocchiari, M.; van Bokhoven, J. A. Catalytic Conversion of Methane to Methanol Using Cu-Zeolites, *Chimia* **2012**, *66*, 668.

(7) Beznis, N. V.; Weckhuysen, B. M.; Bitter, J. H. Cu-ZSM-5 Zeolites for the Formation of Methanol from Methane and Oxygen: Probing the Active Sites and Spectator Species, *Catal. Lett.* **2010**, *138*, 14.

(8) Pappas, D. K.; Martini, A.; Dyballa, M.; Kvande, K.; Teketel, S.; Lomachenko, K. A.; Baran, R.; Glatzel, P.; Arstad, B.; Berlier, G.; Lamberti, C.; Bordiga, S.; Olsbye, U.; Svelle, S.; Beato, P.; Borfecchia, E. The Nuclearity of the Active Site for Methane to Methanol Conversion in Cu-Mordenite: A Quantitative Assessment, *J. Am. Chem. Soc.* **2018**, *140*, 15270.

(9) Grundner, S.; Markovits, M. A. C.; Li, G.; Tromp, M.; Pidko, E. A.; Hensen, E. J. M.; Jentys, A.; Sanchez-Sanchez, M.; Lercher, J. A. Single-site trinuclear copper oxygen clusters in mordenite for selective conversion of methane to methanol, *Nat. Commun.* **2015**, *6*, 7546.

(10) Artiglia, L.; Sushkevich, V. L.; Palagin, D.; Knorpp, A. J.; Roy, K.; van Bokhoven, J. A. In Situ X-ray Photoelectron Spectroscopy Detects Multiple Active Sites Involved in the Selective Anaerobic Oxidation of Methane in Copper-Exchanged Zeolites, *ACS Catal.* **2019**, *9*, 6728.

(11) Dinh, K. T.; Sullivan, M. M.; Serna, P.; Meyer, R. J.; Dinca, M.; Roman-Leshkov, Y. Viewpoint on the Partial Oxidation of Methane to Methanol Using Cu- and Fe-Exchanged Zeolites, *ACS Catal.* **2018**, *8*, 8306.

(12) Groothaert, M. H.; Smeets, P. J.; Sels, B. F.; Jacobs, P. A.; Schoonheydt, R. A. Selective Oxidation of Methane by the Bis(μ-oxo)dicopper Core Stabilized on ZSM-5 and Mordenite Zeolites, *J. Am. Chem. Soc.* **2005**, *127*, 1394.

(13) Groothaert, M. H.; van Bokhoven, J. A.; Battiston, A. A.; Weckhuysen, B. M.; Schoonheydt, R. A. Bis(μ-oxo)dicopper in Cu-ZSM-5 and Its Role in the Decomposition of NO: A Combined in Situ XAFS, UV−Vis−Near-IR, and Kinetic Study, *J. Am. Chem. Soc.* **2003**, *125*, 7629.

(14) Kulkarni, A. R.; Zhao, Z. J.; Siahrostami, S.; Norskov, J. K.; Studt, F. Cation-exchanged zeolites for the selective oxidation of methane to methanol, *Catal. Sci. Technol* **2018**, *8*, 114.

(15) Kvande, K.; Pappas, D. K.; Borfecchia, E.; Lomachenko, K. A. Advanced X-ray Absorption Spectroscopy Analysis to Determine Structure-Activity Relationships for Cu-Zeolites in the Direct Conversion of Methane to Methanol, *Chemcatchem* **2020**, *12*, 2385.

(16) Martini, A.; Signorile, M.; Negri, C.; Kvande, K.; Lomachenko, K. A.; Svelle, S.; Beato, P.; Berlier, G.; Borfecchia, E.; Bordiga, S. EXAFS wavelet transform analysis of Cu-

MOR zeolites for the direct methane to methanol conversion, *Phys. Chem. Chem. Phys.* **2020**, *22*, 18950.

(17) Newton, M. A.; Knorpp, A. J.; Pinar, A. B.; Sushkevich, V. L.; Palagin, D.; van Bokhoven, J. A. On the Mechanism Underlying the Direct Conversion of Methane to Methanol by Copper Hosted in Zeolites; Braiding Cu K-Edge XANES and Reactivity Studies, *J. Am. Chem. Soc.* **2018**, *140*, 10090.

(18) Newton, M. A.; Knorpp, A. J.; Sushkevich, V. L.; Palagin, D.; van Bokhoven, J. A. Active sites and mechanisms in the direct conversion of methane to methanol using Cu in zeolitic hosts: a critical examination, *Chemical Society Reviews* **2020**, *49*, 1449.

(19) Palomino, G. T.; Bordiga, S.; Zecchina, A.; Marra, G. L.; Lamberti, C. XRD, XAS, and IR Characterization of Copper-Exchanged Y Zeolite, *J. Phys. Chem. B* **2000**, *104*, 8641.

(20) Park, M. B.; Ahn, S. H.; Mansouri, A.; Ranocchiari, M.; van Bokhoven, J. A. Comparative Study of Diverse Copper Zeolites for the Conversion of Methane into Methanol, *Chemcatchem* **2017**, *9*, 3705.

(21) Ravi, M.; Sushkevich, V. L.; Knorpp, A. J.; Newton, M. A.; Palagin, D.; Pinar, A. B.; Ranocchiari, M.; van Bokhoven, J. A. Misconceptions and challenges in methane-to-methanol over transition-metal-exchanged zeolites, *Nat. Catal.* **2019**, *2*, 485.

(22) Snyder, B. E. R.; Bols, M. L.; Schoonheydt, R. A.; Sels, B. F.; Solomon, E. I. Iron and Copper Active Sites in Zeolites and Their Correlation to Metalloenzymes, *Chemical Reviews* **2018**, *118*, 2718.

(23) Snyder, B. E. R.; Vanelderen, P.; Bols, M. L.; Hallaert, S. D.; Bottger, L. H.; Ungur, L.; Pierloot, K.; Schoonheydt, R. A.; Sels, B. F.; Solomon, E. I. The active site of low-temperature methane hydroxylation in iron-containing zeolites, *Nature* **2016**, *536*, 317.

(24) Sushkevich, V. L.; Safonova, O. V.; Palagin, D.; Newton, M. A.; van Bokhoven, J. A. Structure of copper sites in zeolites examined by Fourier and wavelet transform analysis of EXAFS, *Chem. Sci.* **2020**, *11*, 5299.

(25) Tomkins, P.; Ranocchiari, M.; van Bokhoven, J. A. Direct Conversion of Methane to Methanol under Mild Conditions over Cu-Zeolites and beyond, *Accounts Chem. Res.* **2017**, *50*, 418.

(26) Zhao, X. L.; Xu, J.; Deng, F. Solid-state NMR for metal-containing zeolites: From active sites to reaction mechanism, *Front. Chem. Sci. Eng.* **2020**, *14*, 159.

(27) Avila Ferrer, F. J.; Cerezo, J.; Stendardo, E.; Improta, R.; Santoro, F. Insights for an Accurate Comparison of Computational Data to Experimental Absorption and Emission Spectra: Beyond the Vertical Transition Approximation, *J. Chem. Theory Comput.* **2013**, *9*, 2072.

(28) Casida, M. E. In *Recent Advances in Density Functional Methods*, p 155.

(29) Rowe, D. J. An intepretation of time-dependent Hartree-Fock theory, *Nucl. Phys.* **1966**, *80*, 209.

(30) Woertink, J. S.; Smeets, P. J.; Groothaert, M. H.; Vance, M. A.; Sels, B. F.; Schoonheydt, R. A.; Solomon, E. I. A $[Cu_2O]^{2+}$ core in Cu-ZSM-5, the active site in the oxidation of methane to methanol, *P. Natl. Acad. Sci. USA* **2009**, *106*, 18908.

(31) Li, H.; Paolucci, C.; Khurana, I.; Wilcox, Laura N.; Göltl, F.; Albarracin-Caballero, J. D.; Shih, A. J.; Ribeiro, F. H.; Gounder, R.; Schneider, W. F. Consequences of exchange-site heterogeneity and dynamics on the UV-visible spectrum of Cu-exchanged SSZ-13, *Chem. Sci.* **2019**, *10*, 2373.

(32) Göltl, F.; Conrad, S.; Wolf, P.; Müller, P.; Love, A. M.; Burt, S. P.; Wheeler, J. N.; Hamers, R. J.; Hummer, K.; Kresse, G.; Mavrikakis, M.; Hermans, I. UV–Vis and Photoluminescence Spectroscopy to Understand the Coordination of Cu Cations in the Zeolite SSZ-13, *Chem. Mater.* **2019**, *31*, 9582.

(33) Salpeter, E. E.; Bethe, H. A. A Relativistic Equation for Bound-State Problems, *Phys. Rev.* **1951**, *84*, 1232.

(34) Blase, X.; Duchemin, I.; Jacquemin, D.; Loos, P.-F. The Bethe–Salpeter Equation Formalism: From Physics to Chemistry, *J. Phys. Chem. Lett.* **2020**, *11*, 7371.

(35) Ipek, B.; Wulfers, M. J.; Kim, H.; Göltl, F.; Hermans, I.; Smith, J. P.; Booksh, K. S.; Brown, C. M.; Lobo, R. F. Formation of $[Cu_2O_2]^{2+}$ and $[Cu_2O]^{2+}$ toward C–H Bond Activation in Cu-SSZ-13 and Cu-SSZ-39, *ACS Catal.* **2017**, *7*, 4291.

(36) Cramer, C. J.; Truhlar, D. G. Density functional theory for transition metals and transition metal chemistry, *Phys. Chem. Chem. Phys.* **2009**, *11*, 10757.

(37) Chan, B.; Gill, P. M. W.; Kimura, M. Assessment of DFT Methods for Transition Metals with the TMC151 Compilation of Data Sets and Comparison with Accuracies for Main-Group Chemistry, *J. Chem. Theory Comput.* **2019**, *15*, 3610.

(38) Harvey, J. N. On the accuracy of density functional theory in transition metal chemistry, *Annu. Rep. Prog. Chem., Sect. C: Phys. Chem* **2006**, *102*, 203.

(39) Hieringer, W.; Görling, A. Failure of time-dependent density functional methods for excitations in spatially separated systems, *Chem. Phys. Lett.* **2006**, *419*, 557.

(40) Marques, M. A. L.; Gross, E. K. U. Time-dependent density functional theory, *Annu. Rev. Phys. Chem.* **2004**, *55*, 427.

(41) Kümmel, S. Charge-Transfer Excitations: A Challenge for Time-Dependent Density Functional Theory That Has Been Met, *Adv. Energy Mater.* **2017**, *7*, 1700440.

(42) Casanova-Páez, M.; Dardis, M. B.; Goerigk, L. ωB2PLYP and ωB2GPPLYP: The First Two Double-Hybrid Density Functionals with Long-Range Correction Optimized for Excitation Energies, *J. Chem. Theory Comput.* **2019**, *15*, 4735.

(43) Casanova-Páez, M.; Goerigk, L. Assessing the Tamm–Dancoff approximation, singlet–singlet, and singlet–triplet excitations with the latest long-range corrected double-hybrid density functionals, *J. Chem. Phys.* **2020**, *153*, 064106.

(44) Goerigk, L.; Casanova-Paéz, M. The Trip to the Density Functional Theory Zoo Continues: Making a Case for Time-Dependent Double Hybrids for Excited-State Problems, *Aust. J. Chem.* **2020**,

(45) Curtis, K.; Panthi, D.; Odoh, S. O. A Time-Dependent DFT Study of Copper (II) Oxo Active Sites for Methane-to-Methanol Conversion in Zeolites, *Inorg. Chem.* **2020**, *submitted*,

(46) Head-Gordon, M.; Rico, R. J.; Oumi, M.; Lee, T. J. A doubles correction to electronic excited states from configuration interaction in the space of single substitutions, *Chem. Phys. Lett.* **1994**, *219*, 21.

(47) Grimme, S.; Neese, F. Double-hybrid density functional theory for excited electronic states of molecules, *J. Chem. Phys.* **2007**, *127*, 154116.

(48) Kim, Y.; Kim, T. Y.; Lee, H.; Yi, J. Distinct activation of Cu-MOR for direct oxidation of methane to methanol, *Chem. Commun.* **2017**, *53*, 4116.

(49) Becke, A. D. Density-functional thermochemistry. III. The role of exact exchange, *J. Chem. Phys.* **1993**, *98*, 5648.

(50) Lee, C.; Yang, W.; Parr, R. G. Development of the Colle-Salvetti correlation-energy formula into a functional of the electron density, *Phys. Rev. B.* **1988**, *37*, 785.

(51) Stephens, P. J.; Devlin, F. J.; Chabalowski, C. F.; Frisch, M. J. Ab Initio Calculation of Vibrational Absorption and Circular Dichroism Spectra Using Density Functional Force Fields, *J. Phys. Chem.* **1994**, *98*, 11623.

(52) Grimme, S.; Antony, J.; Ehrlich, S.; Krieg, H. A consistent and accurate ab initio parametrization of density functional dispersion correction (DFT-D) for the 94 elements H-Pu, *J. Chem. Phys.* **2010**, *132*, 154104.

(53) Grimme, S.; Ehrlich, S.; Goerigk, L. Effect of the damping function in dispersion corrected density functional theory, *J. Comput. Chem.* **2011**, *32*, 1456.

(54) Becke, A. D.; Johnson, E. R. A density-functional model of the dispersion interaction, *J. Chem. Phys.* **2005**, *123*, 154101.

(55) Becke, A. D.; Johnson, E. R. Exchange-hole dipole moment and the dispersion interaction, *J. Chem. Phys.* **2005**, *122*, 154104.

(56) Laun, J.; Vilela Oliveira, D.; Bredow, T. Consistent gaussian basis sets of double- and triple-zeta valence with polarization quality of the fifth period for solid-state calculations, *J. Comput. Chem.* **2018**, *39*, 1285.

(57) Neese, F. Software update: the ORCA program system, version 4.0, *WIRES Comput. Mol. Sci.* **2018**, *8*, e1327.

(58) Hirata, S.; Head-Gordon, M. Time-dependent density functional theory within the Tamm–Dancoff approximation, *Chem. Phys. Lett.* **1999**, *314*, 291.

(59) Jr., T. H. D. Gaussian basis sets for use in correlated molecular calculations. I. The atoms boron through neon and hydrogen, *J. Chem. Phys.* **1989**, *90*, 1007.

(60) Kendall, R. A.; Jr., T. H. D.; Harrison, R. J. Electron affinities of the first-row atoms revisited. Systematic basis sets and wave functions, *J. Chem. Phys.* **1992**, *96*, 6796.

(61) Woon, D. E.; Jr., T. H. D. Gaussian basis sets for use in correlated molecular calculations. III. The atoms aluminum through argon, *J. Chem. Phys.* **1993**, *98*, 1358.

(62) Kossmann, S.; Neese, F. Efficient Structure Optimization with Second-Order Many-Body Perturbation Theory: The RIJCOSX-MP2 Method, *J. Chem. Theory Comput.* **2010**, *6*, 2325.

(63) Weigend, F.; Ahlrichs, R. Balanced basis sets of split valence, triple zeta valence and quadruple zeta valence quality for H to Rn: Design and assessment of accuracy, *Phys. Chem. Chem. Phys.* **2005**, *7*, 3297.

(64) Petrakis, L. Spectral line shapes: Gaussian and Lorentzian functions in magnetic resonance, *J. Chem. Educ.* **1967**, *44*, 432.

(65) Kokotailo, G. T.; Lawton, S. L.; Olson, D. H.; Meier, W. M. Structure of synthetic zeolite ZSM-5, *Nature* **1978**, *272*, 437.

(66) Arvidsson, A. A.; Zhdanov, V. P.; Carlsson, P. A.; Gronbeck, H.; Hellman, A. Metal dimer sites in ZSM-5 zeolite for methane-to-methanol conversion from first-principles kinetic modelling: is the $[Cu\text{-}O\text{-}Cu]^{2+w}$ motif relevant for Ni, Co, Fe, Ag, and Au?, *Catal. Sci. Technol* **2017**, *7*, 1470.

(67) Tsai, M.-L.; Hadt, R. G.; Vanelderen, P.; Sels, B. F.; Schoonheydt, R. A.; Solomon, E. I. [Cu2O]2+ Active Site Formation in Cu–ZSM-5: Geometric and Electronic Structure Requirements for N2O Activation, *J. Am. Chem. Soc.* **2014**, *136*, 3522.

(68) Oord, R.; Schmidt, J. E.; Weckhuysen, B. M. Methane-to-methanol conversion over zeolite Cu-SSZ-13, and its comparison with the selective catalytic reduction of NOx with NH3, *Catal. Sci. Technol* **2018**, *8*, 1028.

(69) Wu, J.-F.; Gao, X.-D.; Wu, L.-M.; Wang, W. D.; Yu, S.-M.; Bai, S. Mechanistic Insights on the Direct Conversion of Methane into Methanol over Cu/Na–ZSM-5 Zeolite: Evidence from EPR and Solid-State NMR, *ACS Catal.* **2019**, *9*, 8677.

(70) Kolganov, A. A.; Gabrienko, A. A.; Yashnik, S. A.; Pidko, E. A.; Stepanov, A. G. Nature of the Surface Intermediates Formed from Methane on Cu-ZSM-5 Zeolite: A Combined Solid-State Nuclear Magnetic Resonance and Density Functional Theory Study, *J. Phys. Chem. C* **2020**, *124*, 6242.

(71) Mahyuddin, M. H.; Tanaka, T.; Shiota, Y.; Staykov, A.; Yoshizawa, K. Methane Partial Oxidation over $[Cu_2(\mu\text{-}O)]^{2+}$ and $[Cu_3(\mu\text{-}O)_3]^{2+}$ Active Species in Large-Pore Zeolites, *ACS Catal.* **2018**, *8*, 1500.

(72) Mahyuddin, M. H.; Staykov, A.; Shiota, Y.; Miyanishi, M.; Yoshizawa, K. Roles of Zeolite Confinement and Cu-O-Cu Angle on the Direct Conversion of Methane to Methanol by $Cu_2(\mu\text{-}O)^{2+}$-Exchanged AEI, CHA, AFX, and MFI Zeolites, *ACS Catal.* **2017**, *7*, 3741.

(73) Mahyuddin, M. H.; Tanaka, T.; Staykov, A.; Shiota, Y.; Yoshizawa, K. Dioxygen Activation on Cu-MOR Zeolite: Theoretical Insights into the Formation of Cu_2O and Cu_3O_3 Active Species, *Inorg. Chem.* **2018**, *57*, 10146.

(74) Yanai, T.; Tew, D. P.; Handy, N. C. A new hybrid exchange–correlation functional using the Coulomb-attenuating method (CAM-B3LYP), *Chem. Phys. Lett.* **2004**, *393*, 51.

(75) Dyballa, M.; Thorshaug, K.; Pappas, D. K.; Borfecchia, E.; Kvande, K.; Bordiga, S.; Berlier, G.; Lazzarini, A.; Olsbye, U.; Beato, P.; Svelle, S.; Arstad, B. Zeolite Surface Methoxy Groups as Key Intermediates in the Stepwise Conversion of Methane to Methanol, *Chemcatchem* **2019**, *11*, 5022.

(76) Sushkevich, V. L.; Verel, R.; van Bokhoven, J. A. Pathways of Methane Transformation over Copper-Exchanged Mordenite as Revealed by In Situ NMR and IR Spectroscopy, *Angewandte Chemie International Edition* **2020**, *59*, 910.

(77) Zheng, J.; Lee, I.; Khramenkova, E.; Wang, M.; Peng, B.; Gutierrez, O. Y.; Fulton, J. L.; Camaioni, D. M.; Khare, R.; Jentys, A.; Haller, G. L.; Pidko, E. A.; Sanchez-Sanchez, M.; Lercher, J. A. Importance of Methane Chemical Potential for Its Conversion to Methanol on Cu-Exchanged Mordenite, *Chem-Eur. J.* **2020**, *26*, 7563.

(78) Odoh, S. O.; Adeyiga, O. Methane Over-Oxidation by Extra-Framework Copper-Oxo Active Sites of Copper-Exchanged Zeolites: Crucial Role of Traps for the Separated Methyl Group, *ChemPhysChem*, *n/a*,

(79) Suleiman, O.; Adeyiga, O.; Panthi, D.; Odoh, S. O. Copper-Oxo Active Sites in the 8MR of Zeolite Mordenite: DFT Investigation of the Impact of Acid Sites on Methanol Yield and Selectivity, *J. Phys. Chem. C* **2021**, *125*,

(80) Dandu, N. K.; Adeyiga, O.; Panthi, D.; Bird, S. A.; Odoh, S. O. Performance of density functional theory for describing hetero-metallic active-site motifs for methane-to-methanol conversion in metal-exchanged zeolites, *J. Comput. Chem.* **2018**, *39*, 2667.

(81) Vogiatzis, K. D.; Li, G.; Hensen, E. J. M.; Gagliardi, L.; Pidko, E. A. Electronic Structure of the $[Cu_3(\mu\text{-}O)_3]^{2+}$ Cluster in Mordenite Zeolite and Its Effects on the Methane to Methanol Oxidation, *J. Phys. Chem. C* **2017**, *121*, 22295.

(82) Ikuno, T.; Grundner, S.; Jentys, A.; Li, G.; Pidko, E.; Fulton, J.; Sanchez-Sanchez, M.; Lercher, J. A. Formation of Active Cu-oxo Clusters for Methane Oxidation in Cu-Exchanged Mordenite, *J. Phys. Chem. C* **2019**, *123*, 8759.

(83) Sushkevich, V. L.; van Bokhoven, J. A. Effect of Brønsted acid sites on the direct conversion of methane into methanol over copper-exchanged mordenite, *Catal. Sci. Technol* **2018**, *8*,

(84) Sushkevich, V. L.; van Bokhoven, J. A. Kinetic study and effect of water on methane oxidation to methanol over copper-exchanged mordenite, *Catal. Sci. Technol* **2020**, *10*, 382.

(85) Zheng, J.; Lee, I.; Khramenkova, E.; Wang, M.; Peng, B.; Gutiérrez, O. Y.; Fulton, J. L.; Camaioni, D. M.; Khare, R.; Jentys, A.; Haller, G. L.; Pidko, E. A.; Sanchez-Sanchez, M.; Lercher, J. A. Importance of Methane Chemical Potential for Its Conversion to Methanol on Cu-exchanged Mordenite, *Chem-Eur. J.* **2020**, *26*, 7515.

For Table of Contents Only

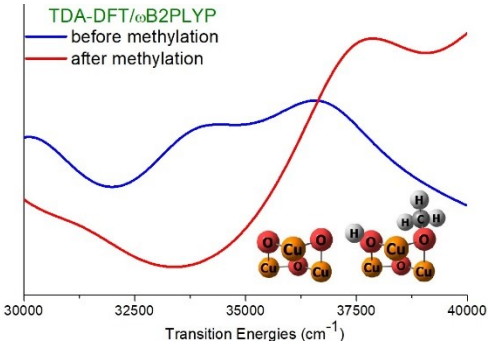

Synopsis: Evolution of the UV-Vis spectra of copper-oxo active sites after methane C-H activation are investigated with TDA-DFT calculations. Our calculations reproduce the spectra of these sites after methane activation. For $[Cu_2O]^{2+}$ and $[Cu_3O_3]^{2+}$, similarities in the computed and experimental spectra is used to ascertain the structure of kinetically trapped intermediates that prevent formation of over-oxidation products. Electronic structure origins of the impact of methane activation on UV-Vis spectra are provided.